References and Notes

1. R. Prins, V. H. J. De Beer, G. A. Somorjai, *Catal. Rev. Sci. Eng.* **31**, 1 (1989).
2. B. Hinnemann *et al.*, *J. Am. Chem. Soc.* **127**, 5308 (2005).
3. T. F. Jaramillo *et al.*, *Science* **317**, 100 (2007).
4. Y. Li *et al.*, *J. Am. Chem. Soc.* **133**, 7296 (2011).
5. X. Zong *et al.*, *J. Am. Chem. Soc.* **130**, 7176 (2008).
6. D. Merki, S. Fierro, H. Vrubel, X. Hu, *Chem. Sci.* **2**, 1262 (2011).
7. G. A. Somorjai, M. A. Van Hove, *Prog. Surf. Sci.* **30**, 201 (1989).
8. S. T. Ceyer, *Annu. Rev. Phys. Chem.* **39**, 479 (1988).
9. G. Ertl, *Angew. Chem. Int. Ed. Engl.* **29**, 1219 (1990).
10. B. Hinnemann *et al.*, *J. Am. Chem. Soc.* **127**, 5308 (2005).
11. J. V. Lauritsen *et al.*, *J. Catal.* **221**, 510 (2004).
12. J. C. Duchet, E. M. van Oers, V. H. J. de Beer, R. Prins, *J. Catal.* **80**, 386 (1983).
13. J. V. Lauritsen *et al.*, *Nat. Nano.* **2**, 53 (2007).
14. L. P. Hansen *et al.*, *Angew. Chem. Int. Ed. Engl.* **50**, 10153 (2011).
15. H. I. Karunadasa, C. J. Chang, J. R. Long, *Nature* **464**, 1329 (2010).
16. F. Gloaguen, T. B. Rauchfuss, *Chem. Soc. Rev.* **38**, 100 (2009).
17. S. J. Smith, C. M. Whaley, T. B. Rauchfuss, S. R. Wilson, *Inorg. Chem.* **45**, 679 (2006).
18. V. J. Murphy, G. Parkin, *J. Am. Chem. Soc.* **117**, 3522 (1995).
19. F. A. Cotton, G. Schmid, *Inorg. Chem.* **36**, 2267 (1997).
20. H. Kopf, S. K. S. Hazari, M. Leitner, *Z. Naturforsch. B: Chem. Sci.* **33b**, 1398 (1978).
21. J. H. Shin, D. G. Churchill, B. M. Bridgewater, K. Pang, G. Parkin, *Inorg. Chim. Acta* **359**, 2942 (2006).
22. J. H. Shin *et al.*, *J. Chem. Soc. Dalton Trans.* **11**, 1732 (2001).
23. A. F. Wells, *Structural Inorganic Chemistry* (Clarendon Press, Oxford, ed. 4, 1975).
24. P. D. Smith, D. A. Slizys, G. N. George, C. G. Young, *J. Am. Chem. Soc.* **122**, 2946 (2000).
25. A. J. Bard, L. R. Faulkner, *Electrochemical Methods* (Wiley, New York, 1980).
26. A. M. Appel, D. L. DuBois, M. R. DuBois, *J. Am. Chem. Soc.* **127**, 12717 (2005).
27. I. Dance, *J. Am. Chem. Soc.* **127**, 10925 (2005).
28. N. Y. Topsoe, H. Topsoe, *J. Catal.* **139**, 641 (1993).
29. M. Frey, *ChemBioChem* **3**, 153 (2002).
30. J. A. Cracknell, K. A. Vincent, F. A. Armstrong, *Chem. Rev.* **108**, 2439 (2008).
31. L. A. Berben, J. C. Peters, *Chem. Commun.* **46**, 398 (2010).
32. B. D. Stubbert, J. C. Peters, H. B. Gray, *J. Am. Chem. Soc.* **133**, 18070 (2011).
33. Y. Sun *et al.*, *J. Am. Chem. Soc.* **133**, 9212 (2011).
34. T. F. Jaramillo *et al.*, *J. Phys. Chem. C* **112**, 17492 (2008).
35. R. M. Kellett, T. G. Spiro, *Inorg. Chem.* **24**, 2378 (1985).
36. B. J. Fisher, R. Eisenberg, *J. Am. Chem. Soc.* **102**, 7361 (1980).
37. P. V. Bernhardt, L. A. Jones, *Inorg. Chem.* **38**, 5086 (1999).

Acknowledgments: Initial synthetic and electrochemical studies were supported by the Department of Energy (DOE) Lawrence Berkeley National Laboratory Helios Solar Energy Research Center (51HE112B to C.J.C.). Further electrochemical studies are based on work performed by the Joint Center for Artificial Photosynthesis, a DOE Energy Innovation Hub, supported through the Office of Science of the U.S. Department of Energy under award DE-SC0004993 (J.R.L.). C.J.C. is an investigator with the Howard Hughes Medical Institute. We thank B. Lassalle, J. Yano, and V. Yachandra for obtaining the x-ray absorption spectroscopy spectra; J. Breen for fabrication of electrochemical cells; Y. Hwang for assistance with gas chromatography; A. T. Iavarone for obtaining the mass spectra; and the University of California President's Postdoctoral Fellowship program for support of E.M. Structural parameters for **1** are available free of charge from the Cambridge Crystallographic Data Centre under identification number CCDC-798834. A patent has been filed by Lawrence Berkeley National Laboratory based on the results presented herein.

Supporting Online Material

www.sciencemag.org/cgi/content/full/335/6069/698/DC1
Materials and Methods
Figs. S1 to S14
Tables S1 and S2
References

27 October 2011; accepted 22 December 2011
10.1126/science.1215868

Near-Field Deformation from the El Mayor–Cucapah Earthquake Revealed by Differential LIDAR

Michael E. Oskin,[1]* J Ramon Arrowsmith,[2] Alejandro Hinojosa Corona,[3] Austin J. Elliott,[1] John M. Fletcher,[3] Eric J. Fielding,[4] Peter O. Gold,[1] J. Javier Gonzalez Garcia,[3] Ken W. Hudnut,[5] Jing Liu-Zeng,[6] Orlando J. Teran[3]

Large [moment magnitude (M_w) ≥ 7] continental earthquakes often generate complex, multifault ruptures linked by enigmatic zones of distributed deformation. Here, we report the collection and results of a high-resolution (≥nine returns per square meter) airborne light detection and ranging (LIDAR) topographic survey of the 2010 M_w 7.2 El Mayor–Cucapah earthquake that produced a 120-kilometer-long multifault rupture through northernmost Baja California, Mexico. This differential LIDAR survey completely captures an earthquake surface rupture in a sparsely vegetated region with pre-earthquake lower-resolution (5-meter–pixel) LIDAR data. The postevent survey reveals numerous surface ruptures, including previously undocumented blind faults within thick sediments of the Colorado River delta. Differential elevation changes show distributed, kilometer-scale bending strains as large as ~10^3 microstrains in response to slip along discontinuous faults cutting crystalline bedrock of the Sierra Cucapah.

Over the past century, most damaging continental earthquakes have arisen from multifault ruptures along incompletely mapped fault arrays (*1*). Quantifying this hazard is limited by inadequate understanding of the mechanisms by which faults link together to generate large earthquakes (*2*) and the difficulty of deducing large, multisegment events from paleoseismic records of ancient fault slip (*3*). Observations of fresh earthquake surface ruptures are critical to unraveling these problems because these most clearly illuminate relations between the paleoseismic record of faulting (at the surface) and seismic energy release that occurs predominantly at depth. In addition to the role of geometric fault segmentation in controlling the potential sizes of earthquakes (*3*), other important relations include the distribution of slip with depth (*4*, *5*) and the related problem of distributed deformation adjacent to faults (*5*–*8*). Well-studied earthquake surface ruptures in California (*9*–*11*) and elsewhere (*12*–*15*) have shown that earlier geologic observations may miss essential components of fault-zone deformation and underestimate the potential for ruptures to jump between faults.

The 4 April 2010 El Mayor–Cucapah sequence is a recent example of a large earthquake generated by a complex, multisegment fault rupture (*16*, *17*). Several faults—many but not all of which were mapped previously (*18*, *19*)—linked together to produce this moment magnitude (M_w) 7.2 earthquake. Because most evidence for ancient fault activity comes from the disruption of landforms by meter-scale fault slip, high-resolution light detection and ranging (LIDAR) topographic surveys (>1 sample/m^2) are valuable for delineating the extent of ancient ruptures, the detailed geometry and offsets in recent earthquakes (*20*), and, thus, the types of earthquakes that are likely to occur in the future. By immediately surveying the El Mayor–Cucapah surface rupture and comparing these measurements to pre-event LIDAR topography collected in 2006 by the Instituto Nacional de Estadística y Geografía (INEGI), we quantify both slip and spatially distributed warping associated with the faults that ruptured together in this earthquake.

To examine differential motion of the ground surface due to the earthquake, we removed the geoid correction from the pre-event LIDAR and subtracted the resulting ellipsoid heights from postevent LIDAR smoothed over a 2.5-m–radius window (*21*). The resulting elevation-difference map shows apparent vertical motion of the ground surface (Fig. 1 and fig. S1). In areas of steep slopes,

[1]Department of Geology, University of California, Davis, 1 Shields Avenue, Davis, CA 95618, USA. [2]School of Earth and Space Exploration, Arizona State University, Tempe, AZ 85287–1404, USA. [3]Centro de Investigación Científica y de Educación Superior de Ensenada, Carretera Ensenada-Tijuana no. 3918, Zona Playitas, C.P. 22860, Ensenada, Baja California, México. [4]Jet Propulsion Laboratory, California Institute of Technology, 4800 Oak Grove Drive, Pasadena, CA 91109, USA. [5]United States Geological Survey, 525 South Wilson Avenue, Pasadena, CA 91106, USA. [6]National Key Laboratory of Earthquake Dynamics, Institute of Geology, China Earthquake Administration, 1# Huayanli, Dewai Avenue, Beijing 100029.

*To whom correspondence should be addressed. E-mail: meoskin@ucdavis.edu

apparent vertical motions are correlated with slope facing direction. This arises from horizontal displacement of topographic ridgelines due to fault slip, as well as from residual systematic distortion present in the pre-event LIDAR survey swaths. We focus here on the elevation alone, for which airborne LIDAR data are most sensitive, in two example areas with extensive pre-event topographic slopes of less than 3°, where the observed elevation-differences are primarily due to tectonic vertical motion of the land surface.

The Paso Inferior accommodation zone (PIAZ) (Fig. 2) illustrates the trade-off in fault slip and distributed deformation among a set of fault strands within the northern Sierra Cucapah. The dominant sense of fault motion here is east-side-down dextral-normal slip, stepping northwestward to structurally lower faults. This pattern mimics the overall rupture throughout the Sierra Cucapah (Fig. 1B), which is more complex in the near-field than inferred from other remote-sensing data (*17*). Nearby outcrops and mapped geologic relations (*19*) indicate that the PIAZ largely involves crystalline bedrock buried by a thin (<<1 km) cover of alluvium. LIDAR-derived elevation differences show how this thinly mantled bedrock deformed in a distributed manner in response to slip along the PIAZ fault array (*21*). Gradients in fault throw (vertical component of slip) determined from fault-scarp mapping and LIDAR-derived elevation differences produce along-fault shear strains, $\gamma \leq 500$ microstrains (μstr). Elevation-differences also reveal that similar magnitudes of strain have accrued via warping between fault strands. For example, profile X-X′ (Fig. 2B and fig. S2) shows 1.1-m net down-to-the-northeast (NE) vertical motion via a combination of 1.6-m throw over two faults, and an overall southwest (SW)–directed tilt that reaches a maximum of 7×10^{-4} radians (rads). The block between the two faults displays an additional component of warping, with tilt ranging from 6×10^{-4} rads SW to 2×10^{-4} rads NE, yielding a bending strain $\gamma = 400$ μstr. Shear strains exceed 1000 μstr as slip trades off between west- and east-dipping faults (fig. S3). These bending strains persist well away (>100 m) from faults observed in the field and mapped from post-event LIDAR. However, small faults with <3 cm of vertical displacement cannot be detected from the LIDAR, and faults with <1 cm of slip were generally not mapped in the field.

Faulting within the PIAZ includes minor SW-down dextral-normal slip along the Laguna Salada fault, which last ruptured in 1892 with up to 5 m of dextral-normal slip, producing an earthquake exceeding M_w 7 (*9*). Surface slip in 2010 along the reactivated portion of the Laguna Salada fault tapers southeastward away from the PIAZ, diminishing to zero within a few hundred meters. Elevation differences adjacent to the Laguna Salada fault show recovery of the 2010 slip via near-field folding (within 200 m of the fault) of the down-thrown block (Fig. 2B). This short-wavelength deformation implies that this fault slip was shallow.

The Indiviso fault zone is a previously unknown array of faults, first detected from radar pixel tracking (*17*), that cut recent sediments of the Colorado River delta. The postevent LIDAR data reveal an unusual style of surface rupture expressed as linear shear zones, 10 to 50 m across, that form kilometer-length curvilinear steps in the elevation of the low-relief delta-plain (Fig. 3). We detect up to 0.5 m of distributed, down to the SW displacement, with maximum tilt approaching 2×10^{-2} rads at the center of the shear zones. This tilt is greater than that observed in the bedrock-dominated Sierra Cucapah, but still too subtle to be detected by traditional field techniques. Detection of lateral slip is generally not possible in the nearly flat landscape. However, where linear cultural features, such as canal levees, cross the Indiviso fault, the LIDAR data are useful for reconstructing their pre-event geometry and determining offsets (fig. S4). We find dextral displacement of similar magnitude (0.5 m) collocated with the zone of vertical deformation. This oblique slip has consistent sense, but lower magnitude than that indicated by far-field observations (*17*).

The shear strains associated with slip along the Indiviso fault are an order of magnitude higher than those observed in between faults in the PIAZ. The paucity of discrete faulting here suggests that unconsolidated, fluid-saturated delta sediments do not localize shear deformation as readily as crystalline rocks and alluvial fan deposits of the Sierra Cucapah. Extensive liquefaction in the delta region, expressed by numerous sandblow and lateral-spreading features, indicates loss of shear strength of the uppermost sediments

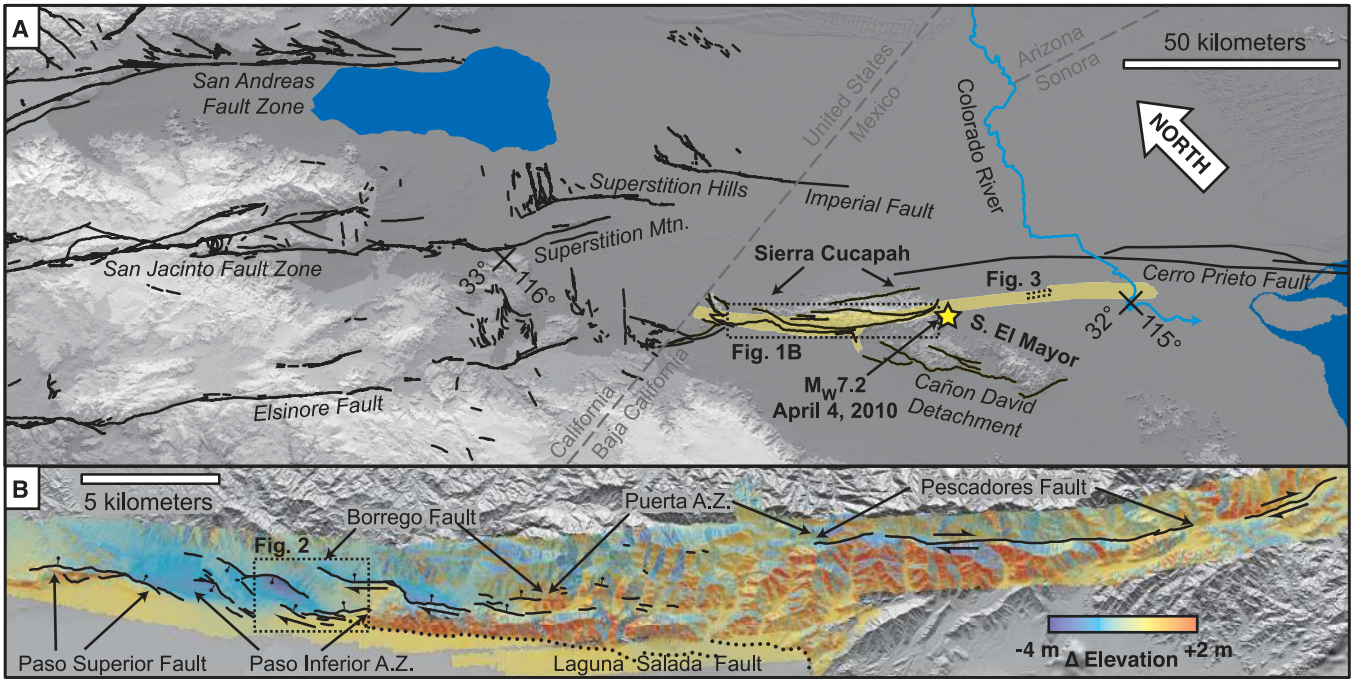

Fig. 1. Setting of El Mayor–Cucapah earthquake surface rupture and LIDAR scan. (**A**) Regional active fault map compiled from pre-earthquake sources (*18*, *19*). The elongate yellow region denotes the extent of the postearthquake LIDAR survey. (**B**) LIDAR-derived height-difference map (post- minus pre-earthquake) for the Sierra Cucapah (see fig. S1 for a more detailed version). Fault ruptures mapped from scarps in postevent LIDAR data are shown as black lines. The black dotted line is the trace of the 1892 Laguna Salada fault rupture (*9*). Distributed deformation across the Paso Inferior and Puerta accommodation zones separate localized slip along principal faults.

during earthquake shaking, which probably contributed to the distributed expression of fault slip here. The uniformity of the width of the zone of folding over several kilometers along strike (Fig. 3) indicates that the fault tip lies at a uniform depth below the surface, consistent with reactivation of an existing, but buried oblique-slip fault.

The comprehensive, near-field deformation illuminated with high-resolution topography and its comparison with pre-event data reveal substantial, shallow, distributed deformation surrounding faults that slipped during the earthquake. An elastic rheology with embedded displacement discontinuities provides a simple model to explain much of the smooth, kilometer-scale warping adjacent to faults (Fig. 2 and figs. S2 and S3). Using a three-dimensional elastic dislocation model (Fig. 2C), with oblique-normal fault slip determined from field observations, we reproduce the overall pattern of subsidence and uplift, as well as key details such as warping of the footwall of the Borrego fault and reactivation of the shallow portion of the Laguna Salada fault due to stress transfer between faults of the PIAZ. Large near-field strains emerge from the interaction of faults that slipped in the shallow crust and greatly exceed the level of strain recovered from interseismic elastic deformation across a single locked fault zone. The differential LIDAR does not directly indicate the processes by which the high strains were accommodated. Coseismic slip along numerous small faults may have led to the observed deformation; however, its close correspondence with modeled surface displacements (Fig. 2B) supports the inference that it arose largely as a direct, elastic response to slip along the mapped, discontinuous major faults of the PIAZ.

Though the distribution of strain we observe is compatible with the elastic dislocation model, its magnitude (>10^3 μstr) may exceed shallow crustal rock strength. Intact granite will indefinitely support elastic shear strains above 3×10^3 μstr in the uppermost crust (*22*), but fractured rock masses are substantially weaker, especially within fault zones (*23*). Near-field distributed deformation from the Landers earthquake apparently changed from elastic to anelastic deformation at ~1 to 2×10^3 μstr (*24*). Coseismic, shallow strains in areas of structural complexity may commonly approach this elastic limit, as implied by steep coseismic slip gradients documented at stepovers (*25*) and where ruptures terminate at asperities (*26*). Because brittle rock strength is time-scale dependent (*22*), large, nearly instantaneous elastic strains induced by coseismic fault slip may be transformed into permanent deformation by dis-

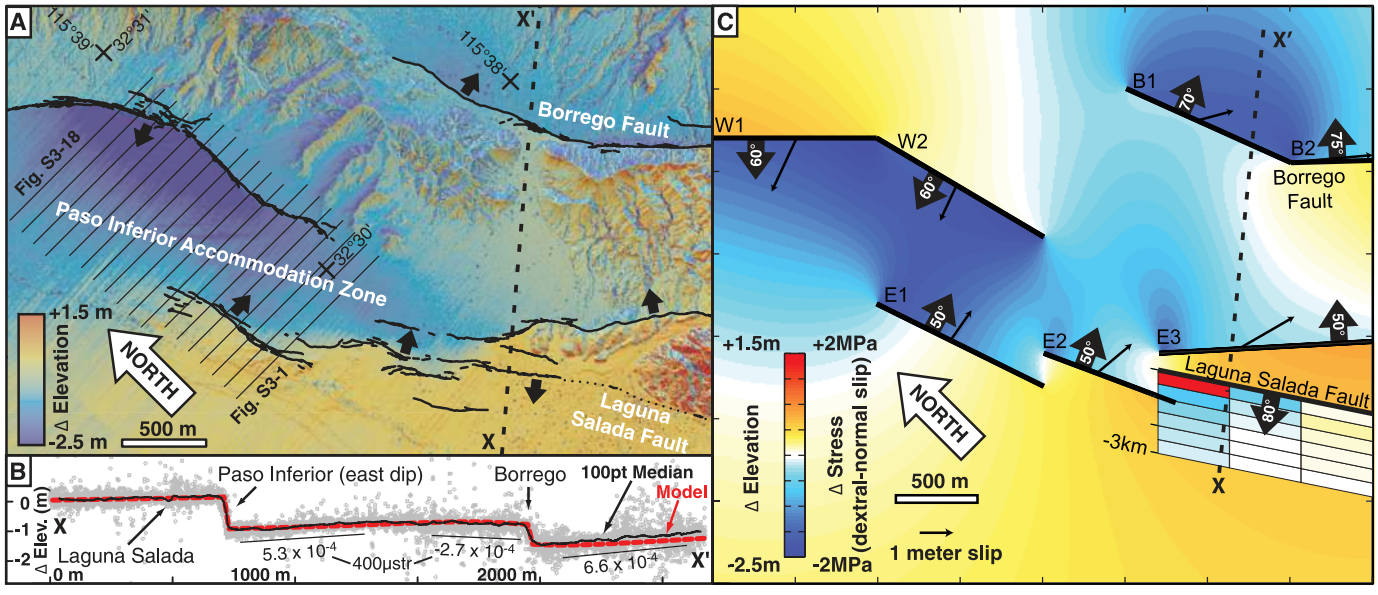

Fig. 2. Differential LIDAR and elastic model of the southern half of the PIAZ. (**A**) Elevation difference map showing distributed deformation as slip steps from the NW Borrego fault into the PIAZ. East-west striping in height difference reflects noise in the pre-event LIDAR. Black arrows show fault dip direction. (**B**) Swath profile of elevation difference along line X-X′ in (A). Points are within 50 m of the line as plotted. Outlier points result from noise and lateral displacement of locally steeper topography and vegetation (fig. S2). (**C**) Elastic model, using rectangular dislocations (table S1) and Poisson's ratio of 0.3, constructed in Coulomb (*31*), showing vertical surface deformation due to imposed slip along the PIAZ fault array. The model does not reproduce fault-slip gradients, and some faults extend beyond the domain shown. Slip vectors point in the direction of motion of the fault hanging wall. Modeled slip vectors match field observations of fault slip in the area shown, with the exception of faults E1 to E3, where normal slip is 30% above the observed values to match the elevation-difference map. Coulomb stress change for oblique dextral-normal slip (rake 135°) along the Laguna Salada fault is shown for 500-by-500–m patches, from the surface to 3-km depth, projected to the surface. Stress was calculated with a shear modulus of 3 GPa, which is appropriate for damaged fault-zone rock (*23*).

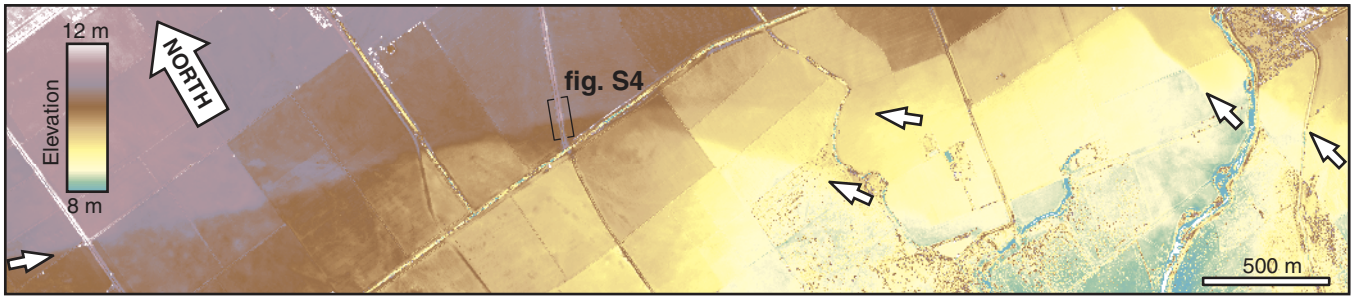

Fig. 3. Postearthquake LIDAR-derived topography (4 m of total relief) along a portion of the Indiviso fault (see Fig. 1 for location). Arrows highlight end points of shear zones recognized from topographic steps. Other elevation steps and lineaments are canals or boundaries of leveled agricultural fields.

tributed yielding mechanisms, such as granular flow (*5*, *6*) or velocity-strengthening slip along pervasively distributed fractures (*27*). Distributed yielding is commonly expressed along faults as fault-related folds, rock fabrics, topographic uplift, and gradients in cumulative slip and slip-rate (*8*, *28*–*30*). The time scale of this distributed yielding could be essentially coseismic or take months, and it may be difficult to distinguish from other coseismic deformation. Postseismic dilatancy recovery (*6*) could provide indirect evidence of its occurrence.

If a substantial fraction of plate-boundary motion is absorbed as distributed deformation in zones of structural complexity, surface rupture and strong ground motion hazard may be underpredicted. Paleoseismic measurements will underestimate fault slip rates at depth due to this unaccounted deformation. In addition to slip rate, maximum earthquake size may also be misjudged due to incomplete knowledge of the linkages between faults. These problems modestly affect hazard from fast-slipping, well-localized primary plate-boundary faults but can lead to severe underestimation of hazard away from primary faults where large (>M_w 7) earthquakes along secondary fault arrays dominate strong ground motions (*1*). As exemplified by the highly segmented El Mayor–Cucapah surface rupture and similarly sized historic events in southern California (*9*–*11*), anticipating the sizes of the largest earthquakes along secondary fault arrays and the shaking and rupture hazards that these pose to critical facilities and lifelines requires careful attention to the extent and connectivity of mapped active faults. Scarp-forming paleoearthquakes along short fault segments, accompanied by large along and off-fault strains, provide key hazard information, as such events probably involved adjacent fault segments as parts of a larger surface rupture.

References and Notes

1. P. England, J. Jackson, *Nat. Geosci.* **4**, 348 (2011).
2. R. Harris, S. Day, *Geophys. Res. Lett.* **26**, 2089 (1999).
3. S. G. Wesnousky, *Nature* **444**, 358 (2006).
4. G. King, S. Wesnousky, *Bull. Seismol. Soc. Am.* **97**, 1833 (2007).
5. Y. Fialko, D. Sandwell, M. Simons, P. Rosen, *Nature* **435**, 295 (2005).
6. E. J. Fielding, P. R. Lundgren, R. Bürgmann, G. J. Funning, *Nature* **458**, 64 (2009).
7. W. Huang, A. Johnson, *J. Geophys. Res.* **115**, B03408 (2010).
8. E. Shelef, M. Oskin, *J. Geophys. Res.* **115**, B05308 (2010).
9. K. Mueller, T. Rockwell, *Bull. Geol. Soc. Am.* **107**, 8 (1995).
10. K. Sieh *et al.*, *Science* **260**, 171 (1993).
11. J. Treiman, K. Kendrick, W. Bryant, T. Rockwell, S. McGill, *Bull. Seismol. Soc. Am.* **92**, 1171 (2002).
12. J. Liu-Zeng *et al.*, *Bull. Seismol. Soc. Am.* **100**, 2615 (2010).
13. P. Haeussler *et al.*, *Bull. Seismol. Soc. Am.* **94**, S23 (2004).
14. Y. Klinger *et al.*, *Bull. Seismol. Soc. Am.* **95**, 1970 (2005).
15. M. Berberian *et al.*, *Geophys. J. Int.* **136**, 671 (1999).
16. E. Hauksson *et al.*, *Pure Appl. Geophys.* **168**, 1255 (2011)
17. S. Wei *et al.*, *Nat. Geosci.* **4**, 615 (2011).
18. C. Jennings, *Fault Activity Map of California and Adjacent Areas, with Locations and Ages of Recent Volcanic Eruptions*, scale 1:750,000, *Geologic Data Map no. 6* (California Division of Mines and Geology, Sacramento, CA, 1994).
19. J. Fletcher, R. Spelz, *Geosphere* **5**, 385 (2009).
20. K. Hudnut, A. Borsa, C. Glennie, J. Minster, *Bull. Seismol. Soc. Am.* **92**, 1570 (2002).
21. Materials and methods are available on *Science* Online.
22. D. A. Lockner, *J. Geophys. Res.* **103**, 5107 (1998).
23. E. Cochran *et al.*, *Geology* **37**, 315 (2009).
24. R. Michel, J. Avouac, *J. Geophys. Res.* **111**, B03408 (2006).
25. A. J. Elliott, J. F. Dolan, D. D. Oglesby, *J. Geophys. Res.* **114**, B02313 (2009).
26. I. Manighetti, M. Campillo, C. Sammis, P. Mai, G. King, *J. Geophys. Res.* **110**, B05302 (2005).
27. C. Marone, C. Scholz, *Geophys. Res. Lett.* **15**, 621 (1988).
28. J. Kaven, S. Martel, *J. Struct. Geol.* **29**, 1463 (2007).
29. E. Kirby *et al.*, *Tectonics* **26**, TC2010 (2007).
30. K. Blisniuk *et al.*, *J. Geophys. Res.* **115**, B08401 (2010).
31. S. Toda, R. Stein, J. Lin, V. Sevilgen, Coulomb 3 stress change modeling software, http://earthquake.usgs.gov/research/modeling/coulomb.

Acknowledgments: LIDAR data acquisition supported by an NSF RAPID grant (EAR-1039168 and 1039147), with additional support from the Southern California Earthquake Center (supported by NSF-EAR-0106924 and U.S. Geological Survey grant 02HQAG0008) and Consejo Nacional de Ciencia y Tecnología (grant CB-2007-81463). Part of this research was supported by NASA's Earth Surface and Interior Focus Area and performed at the Jet Propulsion Laboratory, California Institute of Technology. Y. Fialko, D. Sandwell, J. Galetzka, and A. Gonzalez assisted with Global Positioning System data acquisition and processing. C. Crosby, D. Haddad, O. Kreylos, A. Morelan, and T. Sato provided editorial and computational assistance. The National Center for Airborne Laser Mapping gathered and processed the postevent LIDAR data, distributed at OpenTopography (http://opentopography.org/id/OTLAS.122010.32611.1). We thank INEGI for granting access to the pre-event LIDAR data used for this study. Pre-event LIDAR digital elevation model and derived elevation difference data for the Sierra Cucapah rupture zone are available in the supporting online material.

Supporting Online Material

www.sciencemag.org/cgi/content/full/335/6069/702/DC1
Materials and Methods
Figs. S1 to S4
Table S1
Databases S1 and S2

9 September 2011; accepted 13 January 2012
10.1126/science.1213778

Propagation of Slow Slip Leading Up to the 2011 M_w 9.0 Tohoku-Oki Earthquake

Aitaro Kato,* Kazushige Obara, Toshihiro Igarashi, Hiroshi Tsuruoka, Shigeki Nakagawa, Naoshi Hirata

Many large earthquakes are preceded by one or more foreshocks, but it is unclear how these foreshocks relate to the nucleation process of the mainshock. On the basis of an earthquake catalog created using a waveform correlation technique, we identified two distinct sequences of foreshocks migrating at rates of 2 to 10 kilometers per day along the trench axis toward the epicenter of the 2011 moment magnitude (M_w) 9.0 Tohoku-Oki earthquake in Japan. The time history of quasi-static slip along the plate interface, based on small repeating earthquakes that were part of the migrating seismicity, suggests that two sequences involved slow-slip transients propagating toward the initial rupture point. The second sequence, which involved large slip rates, may have caused substantial stress loading, prompting the unstable dynamic rupture of the mainshock.

Laboratory and theoretical studies have proposed that earthquakes are preceded by a nucleation process where stable, slow rupture growth develops into unstable, high-speed rupture within a confined zone on a fault (*1*–*5*). The nucleation process has been discussed actively in association with the occurrence of foreshocks near the mainshock hypocenters and the presence of short-duration initial phases in the records of some earthquake events (*6*–*10*). A recent study on the 1999 moment magnitude (M_w) 7.6 Izmit, Turkey, earthquake suggested the possibility that the mainshock was preceded, for 44 min, by a phase of slow slip at the base of the brittle crust (*11*). If this kind of premonitory slow-slip behavior also precedes other large earthquakes, its knowledge should have crucial implications for earthquake prediction and risk assessment. It is, therefore, essential to scrutinize seismic records of other large, well-recorded earthquakes in search of similar nucleation processes.

The 11 March 2011 Tohoku-Oki earthquake was the first M_w 9 event to be recorded by a dense network of continuous and broad–frequency-range seismic stations. The extremely large spatial extent of the event (up to ~500 km) is expected to help study how it nucleated, providing an invaluable opportunity to elucidate preparatory processes for earthquake generation. The Tohoku-Oki earthquake ruptured a megathrust fault off the eastern shore of northern Honshu, Japan, where the Pacific plate is subducting beneath a continental plate at a convergence rate of 10 cm/year. According to the Japan Meteorological Agency (JMA) catalog, the mainshock was preceded by foreshock sequences lasting 23 days (*12*), starting with a burstlike seismicity in mid-February. The largest foreshock was a M_w 7.3 event that took

Earthquake Research Institute, The University of Tokyo, Tokyo, Japan.

*To whom correspondence should be addressed. E-mail: akato@eri.u-tokyo.ac.jp